International Journal of Heat and Mass Transfer 179 (2021) 121644

Contents lists available at ScienceDirect

International Journal of Heat and Mass Transfer

journal homepage: www.elsevier.com/locate/hmt

Effect of time and spatial domains on monolayer 2D material interface thermal conductance measurement using ns ET-Raman

Nicholas Hunter[a,1], Hamidreza Zobeiri[a,1], Tianyu Wang[b,*], Xinwei Wang[a,*]

[a] Department of Mechanical Engineering, Iowa State University, 2025 Black Engineering Building, Ames, IA 50011, USA
[b] Institute of Chemistry, Chinese Academy of Science, Beijing 100190, PR China

ARTICLE INFO

Article history:
Received 13 March 2021
Revised 7 June 2021
Accepted 25 June 2021

Keywords:
Monolayer
2D materials
Interfacial thermal resistance
Energy transport state design
Nanosecond Raman

ABSTRACT

Raman-based approaches to characterizing thermal properties of nanoscale and microscale materials have proven to be powerful experimental methods. This work explores the potential of energy-transport state-resolved Raman (ET-Raman) for the precise determination of interfacial thermal conductance (G) between monolayer 2D materials and their substrates. ET-Raman employs a continuous wave laser and nanosecond (ns) pulsed laser to induce both steady state and transient heating while simultaneously collecting 2D material temperature information from the Raman signal. A 3D numerical model built using the finite volume method simulates the two differentiated thermal transport processes. The simulated temperature rises are compared with experimental Raman temperature information to extract G. In this study, we investigate the temporal effects of the pulse frequency and pulse width of the ns laser on precise characterization of G. By running multiple simulations for a range of pulsed laser frequencies and pulse widths, we determine that ET-Raman is most sensitive to precise interfacial thermal conductance measurements with short pulse widths (~below 20 ns) and with pulsing frequencies that ensure sufficient cooling time between consecutive pulses (~below 500 kHz). We also conclude that substrate thickness and laser spot size play critical roles in heat distribution and subsequent sensitivity to meaningful G measurements. As both laser spot size and SiO_2 substrate thickness decrease, detection of interfacial thermal transport becomes more difficult. These results offer essential guidance in the design of future Raman-based approaches to thermal measurements using pulsed lasers.

1. Introduction

The physics of two-dimensional (2D) materials continues to intrigue nanoscience researchers and provide new opportunities for fundamental and applied research. The evolving body of knowledge has already proven 2D materials such as graphene and transition metal dichalcogenides (TMDs) have applications as photodetectors, photovoltaic solar cells, light-emitting diodes, and high-performance chemical sensors due to their unique electrical properties [1–3]. In addition, the thermal properties of graphene alone have made it a promising material for thermal management and energy storage devices [4,5].

However, heat transfer at the interface between 2D materials and substrates thwarts the full realization of these applications in future nanoscale technologies. The phonon mean free path in nanoscale systems often matches or exceeds the length scale of 2D material-based devices. This introduces unprecedented obstacles to the design of efficient thermal control mechanisms due to the emergence of interfacial scattering, ballistic transport, and wave-effects often causing the interfacial thermal resistance to disproportionally govern the thermal transport of the entire system [6].

Surface chemistry and interface coupling dictate the properties and performance of 2D materials in nanoelectronics as well. Low-resistance electrical contacts require strong interfacial interactions and it has been proven that increasing the bonding strength between dissimilar materials results in more phonon coupling across the interface [7,8]. Clearly, it is still true that “the interface is the device” [9].

Given the significance of interfaces in nanostructured systems, the measurement and control of interfacial thermal resistance R''_{tc} (i.e. conductance $G = 1/R''_{tc}$) receives much academic attention and Raman spectroscopy serves as a powerful tool to investigate this property. One popular technique involves passing an electrical current through the 2D material and monitoring the temperature rise via the temperature dependant Raman signal. This method requires

---

* Corresponding authors.
E-mail addresses: tywang@iccas.ac.cn (T. Wang), xwang3@iastate.edu (X. Wang).

[1] These authors contributed equally to this work.

https://doi.org/10.1016/j.ijheatmasstransfer.2021.121644

precise calibration of the Raman temperature coefficient beforehand. The resistance is solved for analytically once the temperature difference between the 2D material and substrate has been distinguished for a given amount of electrical power. This Raman thermometry through Joule heating technique has been used to study a variety of interfaces such as graphene/h-Bn, MoS_2/h-Bn, and graphene/4H-SiC [10–12].

The optothermal Raman method is also widely used by researchers to measure interfacial thermal resistance [13–15]. Instead of Joule heating, laser irradiation acts as the heating source while also providing the Raman temperature characterization. First developed in 2008 to measure the thermal conductivity of single-layer graphene, the optothermal Raman method succeeds at interfacial conductance measurements as well [5]. After Raman temperature coefficient determination and estimation of the absorbed laser power density, a heat transfer model based on the cylindrical heat equation is used alongside the experimental Raman temperature data to extract the interface thermal resistance.

Additionally, a comprehensive optothermal Raman method using continuous wave and pulsed lasers has been developed to measure the thermal properties of monolayer materials. Zhang et al. extracted the specific heat and thermal conductivity of monolayer graphene (both supported and suspended) by comparing Raman temperature information from different combinations of laser spot size and pulse duration [16]. By creating temperature rise ratios out of steady state heating at different laser spot radii as well as transient heating at different pulse durations, they were able to use normalized ratio parameters from which thermal property information could be extracted without needing a laser absorption coefficient (a variable that often introduces non-negligible error to most Raman-based methods).

The dual-wavelength flash Raman mapping method is another powerful technique that eliminates the need for laser absorption and reliably measures thermophysical properties of 2D nanomaterials [17,18]. This method employs a periodical heating laser alongside a different wavelength probing laser. By adjusting the time separation between heating and probing pulses, the varying temperature responses of the 2D material can be compared. These temperature variations are then used with a 2D transient heat conduction model to extract thermal diffusivity.

These Raman-based techniques all offer unique advantages for experimentalists wanting to accurately measure thermophysical properties of nanoscale materials. They also have the benefit of being cost-effective and relatively simple to use. More so for the optothermal method, sample preparation is also quite straightforward. However, the Raman temperature coefficient calibration required in all these techniques can introduce non-negligible error to the final experimental results which is often overlooked [19]. Calibration of the Raman temperature coefficient occurs through a different heating process than that of the experimental measurement. Traditionally, calibration involves uniform heating of the sample of interest and its substrate. The 2D material and substrate are gradually brought to the same temperature. The Raman signal is then measured at different temperatures. This scenario involves minimal thermal stress in the material of interest. On the other hand, during laser heating, the Gaussian-shaped laser beam inevitably creates a temperature gradient in the 2D material which causes thermal stress in the radial direction. Also the temperature difference between the 2D material and substrate during laser heating causes another stress because of the large thermal expansion mismatch between them. This thermal stress can influence the Raman shift peak location. Thus, the Raman signal temperature dependency determined during calibration and then used for analysis does not accurately represent the thermal transport under investigation. Additionally, measuring the laser absorption in 2D materials can be problematic, especially for supported samples, leading to further uncertainty in temperature measurements since absorbed laser power is often estimated [13,15].

The energy transport state-resolved Raman (ET-Raman) technique circumvents the previously mentioned sources of uncertainty in G measurements. This technique is described by the creation of multiple energy transport states via the variation of laser heating sources (CW and pulsed) and laser spot sizes (changing objective lenses). The differentiated energy transport states facilitate the extraction of thermal property information. Our previous works have employed various combinations of CW, nanosecond, and picosecond lasers to measure a range of nanomaterial thermal properties such as the thermal conductance between water and nm-thick WS_2 and the nonequilibrium temperature distribution of optical and acoustic phonons in 2D materials after laser irradiation (MoS_2, $MoSe_2$, and graphene paper) [20–23].

The ET-Raman method reduces measurement uncertainties by eliminating both Raman temperature coefficient calibration and laser absorption effects (discussed in the upcoming section). Furthermore, the radiative electron-hole recombination inherent to monolayer TMD materials is accounted for in thermal transport characterization. Due to the indirect to direct band gap transition as TMD materials go from bulk to single layer, excitons in monolayer TMD materials recombine radiatively and nonradiatively [24]. Therefore, not all absorbed laser energy contributes to thermal processes in the 2D material-substrate system. Disregarding the radiative recombination leads to overestimated thermal conductance measurements. In our previous work investigating the rate of radiative decay, using ET-Raman we determined the radiative recombination efficiency β and interfacial thermal conductance G of WSe_2 monolayers on fused silica substrate [21].

Unlike the pump-probe technique in which the transient temperature decay is measured in the time domain using two lasers, ET-Raman only requires one pulsed laser to study transient thermal diffusion. Depending on the frequency and pulse width, the pulsed laser can cause transient as well as accumulated heating effects. ET-Raman considers both effects in an integrated, comprehensive treatment of the 2D material temperature rise.

Generally, the laser pulse width and repetition rate play critical roles in determining how sensitive G is to accurate measurement. The pulse width controls the thermal diffusion length into the sample and the repetition rate (i.e. the cooling time between consecutive pulses) dictates the degree to which heating accumulates in the sample. These features of a pulsed laser cannot be easily described by analytical solutions. Rather, pulse width and repetition rate can be encompassed in the numerical modelling of 3D transient heat conduction to uncover their role in experimental measurements of interfacial thermal conductance.

This work examines the role of temporal laser pulse features as they apply to the 3D finite volume laser heating model used for the ET-Raman method. The context of the physical model is the determination of interfacial thermal conductance G between monolayer WSe_2 and fused silica substrate. Our previous work reports the experimental results of this measurement while this work primarily focuses on elucidating the sensitivity of the ET-Raman method to high accuracy G determination. Generally, we find that shorter laser pulse widths lead to more accurate measurements. We also determine that high frequency pulsing lowers the sensitivity to meaningful G measurement. Lastly, we explore how these same pulse features influence G measurements when the monolayer is supported by an SiO_2/Si substrate. The work reported here serves as a helpful guide in the development of future ET-Raman experiments using pulsed lasers to study transient nanoscale heat transfer.

2. Physics principles of ET-Raman and general picture of various parameters

A. Physics of energy transport states in ET-Raman

The ET-Raman technique exploits the temperature dependence of Raman vibrational modes. As the 2D material temperature increases, due to bond softening the Raman signal red-shifts. In the context of single layer WSe_2, the Raman peak signal of interest is the degenerate A_{1g} and E_{2g}^1 first order modes at 250 cm^{-1} in the Raman spectrum [25]. As the laser power incident on the monolayer increases, the growing temperature rise causes Raman redshift. The rate of red-shift is defined as the laser power differential $\psi = \partial\omega/\partial P$. This parameter, defined as the Raman shift coefficient (RSC), is directly proportional to the local temperature rise in the sample under unit power laser irradiation. It is also related to the Raman temperature coefficient ($\partial\omega/\partial T$) and laser absorption ($\alpha$) – two critical variables for optothermal Raman measurements. Both $\partial\omega/\partial T$ and α vary widely between samples and introduce nontrivial uncertainty in extracted temperature information. However, taking the ratio of two laser power differentials from different laser sources, such as nanosecond (ns) and continuous wave (CW) lasers, nullifies the effect of these sample-dependant variables on the extracted temperature information.

As illustrated in Fig. 1a,b, the CW and ns lasers induce distinct heating phenomena: The ns laser provides transient heat conduction with a drastically reduced heat diffusion length into the substrate while the CW laser maintains steady state heating with a much larger heat diffusion length. Thus, the RSC from each laser source contains unique information related to the differentiated sample temperature rises.

The RSC is determined by incrementally increasing the power of the irradiating laser (ΔP) while measuring the red-shifting Raman peak signal ($\Delta\omega$). In experiments, this is accomplished using a motorized rotating neutral density filter that varies the laser transmission. The Raman signal red-shift exhibits a negative linear relationship with increasing laser power (for the low power range). The slope of a fitted trend line becomes the experimental Raman shift coefficient as$\psi = \Delta\omega/\Delta P = \partial\omega/\partial P$.

In our previous work, we show that the RSC ratio ψ_{ns}/ψ_{CW} can be used in conjunction with thermal modelling to extract the interfacial thermal conductance between monolayer WSe_2 and fused silica [21]. The 3D finite volume heating model used necessitates special consideration of the laser energy distribution in the space and time domains. Because the laser spot spatial energy distribution on the WSe_2 sample is Gaussian-shaped, the Raman scattered light detected by the spectrometer is not directly proportional to the absolute temperature rise of the material. Instead, to extract local temperature information from the RSC, a Raman intensity weighted average temperature of the WSe_2 monolayer must be derived. This concept of a Raman weighted average temperature rise is pictorially represented in Fig. 1c–e.

In the CW case this is formulated as an integral evaluated over the heating volume (V) of interest: $\overline{T}_{WSe_2,CW} = \int_0^V Ie^{-z/\tau_L} T dv / \int_0^V Ie^{-z/\tau_L} dv$. I is the Gaussian-distributed CW laser intensity in the material, T is the temperature, z is the distance from the sample surface, and τ_L is the absorption depth of the material. The exponential term accounts for intensity attenuation as Raman signal passes through the material. Note that the laser intensity term can be expanded as $I = I_0 \exp(-r^2/r_0^2)\exp(-z/\tau_L)$ where I_0 is the laser peak intensity (set to 0.1 mW during numerical modelling) and r_0 is the laser spot radius. As shown in Fig. 1c, in the radial direction, the laser intensity and the temperature rise follow different profiles. The temperature rise has a broader distribution due to heat conduction, and the Raman measurement only measures the part within the heating region weighted by the Raman intensity. The ns case yields a similar integral that must be integrated over the space domain (due to the Gaussian spatial energy distribution) and the time domain (due to the pulsed nature of the ns laser): $\overline{T}_{WSe_2,ns} = \int_0^t \int_0^V Ie^{-z/\tau_L} T dv dt / \int_0^t \int_0^V Ie^{-z/\tau_L} dv dt$ where I is now the ns laser intensity. As shown in Fig. 1b, the temperature rise profile in the time domain could be significantly different from that of the laser intensity. Therefore, the measured Raman shift change in the ns case rather reflects temperature rise within the laser heating time weighted by the Raman intensity. Note here the laser intensity distribution in the thickness direction of the sample is simplified without considering the scattering and interference effect. The Raman signal generation is proportional to the local laser intensity, but its scattering and interference effect is also not considered. This will not have an effect on our thermal modelling treatment since the sample is monolayer and the temperature is uniform across the thickness. For thicker samples, strict treatment of the laser and Raman signal interference effect in the sample can be realized using our rigorous model that considers the discontinuity of Raman signal within the sample [26].

B. Effects of laser spot size, pulse width, and pulse interval: a general picture

Experimental design of the ET-Raman method necessitates careful consideration of three critical parameters: Size of the heating area, pulse width of the ns laser, and the time interval between pulses. These three parameters govern the thermal transport caused by laser heating as well as the subsequent sensitivity in experimentally measuring R''_{tc}.

The volume of sample undergoing laser heating is tightly related to the interfacial thermal resistance measurement sensitivity. CW laser irradiation causes essentially infinite heat diffusion into the substrate. While the ns laser has a more restricted diffusion length. Both laser sources induce unique and separate thermal transport that differentiate the prominence of the interfacial thermal resistance in overall system heating. To be clear, the interfacial thermal resistance does not change between the two laser heating scenarios – only the sensitivity to measurement. This is because the substrate thermal resistance disproportionally impacts the overall heating in the CW case, masking the heating effect caused by the resistance at the interface. This disproportionate contribution from the substrate resistance is mitigated during ns heating.

Under CW laser heating the total interface resistance, calculated as $R_T \sim 4R''_{tc}/\pi D^2$, is determined by the interfacial thermal resistance per unit area R''_{tc} and the diameter of the heating area D. The value of the substrate resistance is evaluated using the appropriate shape factor for heat conduction through a disk with diameter D: $R_S \sim 1/2Dk_s$ Where k_s is the thermal conductivity of the substrate [27]. The diameter of the cylindrical heated area is simply defined as the diameter of the laser spot on the sample surface (the radial heat diffusion is negligible within the laser heating area). Note that the substrate resistance R_S depends on the factor D^{-1} while the total interface resistance R_T depends on D^{-2}. It follows that changing the diameter of the laser spot alters the relative importance of the interfacial resistance. As the laser spot increases, R_T will decrease quicker than R_S meaning the relative contribution from resistance at the interface becomes less significant.

The ns laser source does not produce the same thermal response making the interfacial thermal resistance more sensitive to measurement. A pulsed laser source yields a substrate resistance evaluated as $R_S \sim 4L_T/k_s\pi D^2$ where L_T is the heat diffusion length. Now, both R_T and R_S depend on a factor of D^{-2}. Thus, changes in

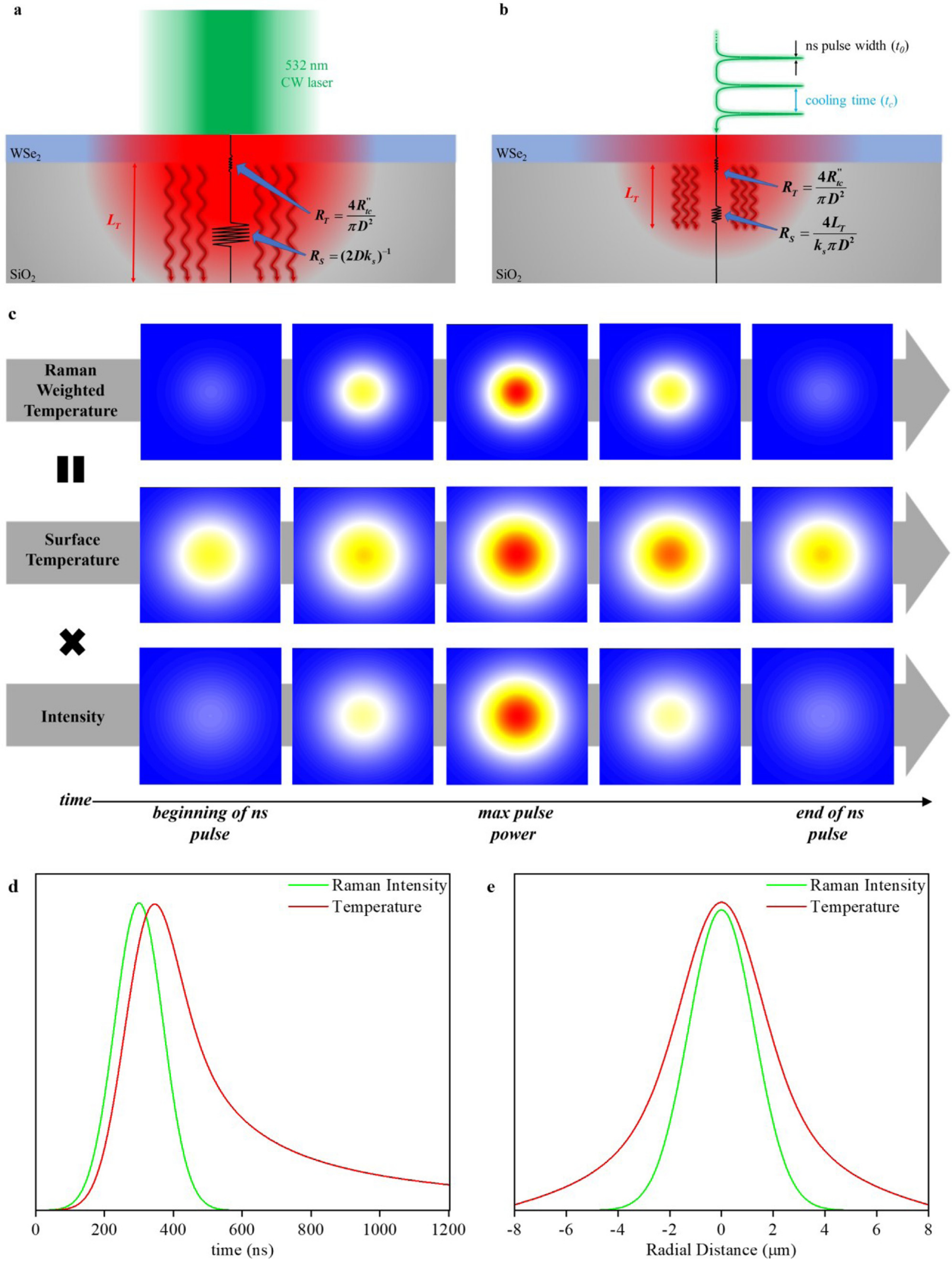

Fig. 1. (a) Physical diagram of CW laser heating where the substrate thermal resistance dominates the heating of the sample-substrate system. (b) ns laser heating diagram when the substrate resistance becomes more comparable to the interfacial thermal resistance. (c) Physical conceptualization of the Raman intensity weighted temperature rise during a single ns laser pulse. The weighting is integrated over the time and space domains for ns ET-Raman, and only the space domain in the CW case. (d) The intensity of a single ns laser pulse and the subsequent sample temperature rise in the time domain. (e) 1D radial contour of the intensity and temperature spatial distribution during both CW and ns laser irradiation.

the heating area diameter do not change the relative importance of the interfacial thermal resistance as strongly as they do in the CW laser heating case. However, it is important to note that the heat diffusion length does play a critical role in the resulting sensitivity to measurement. Clearly, as the heat diffusion length gets smaller the substrate resistance shrinks leading to a growth in the relative prominence of the interfacial thermal resistance. This heat diffusion length, estimated as $L_T \approx 2\sqrt{t_0 \alpha}$, is dependant on the substrate thermal diffusivity α and the ns laser pulse width t_0. Therefore, theoretically it is expected that as the ns laser pulse width decreases the substrate thermal resistance becomes less significant in the total heating and the interfacial thermal resistance becomes more sensitive to precise measurement.

Lastly, the interval between pulses (i.e. the repetition rate) needs to be accounted for in the design of an ET-Raman experiment using a pulsed laser. If transient states of heat conduction are desired, then the interval between consecutive pulses needs to be long enough that the material cools down completely to ambient temperature. This crucial cool down time is necessary to distinguish the CW steady state heating from the transient ns pulsed laser heating. R''_{tc}becomes much more sensitive to accurate measurement with this differentiation of thermal transport. If the interval between pulses becomes too short – meaning a faster repetition rate – the pulsed laser heating effectively becomes more like CW laser heating since there will be an accumulated temperature rise over the course of multiple pulses.

The drawback to choosing a slow repetition rate with enough time for the laser heated sample to return to thermal equilibrium between pulses is the lower average power output. A reduced average laser power will not stimulate sufficient Raman scattering in the sample. The weaker Raman signal prevents accurate measurement of the interfacial thermal conductance since the ET-Raman method requires precise Gaussian fitting of a Raman peak. Therefore, a successful experimental setup requires a thoughtful balance between a repetition rate that guarantees transient heating conditions while still exciting strong Raman signal.

3. Heat conduction treatment for CW and transient state

Because the ET-Raman method combines computational and analytical methods, the treatment of the heat conduction through the sample-substrate entails both methods as well. More specifically, the theoretical 2D material temperature is determined via numerical modelling and analytical solving. The atomically thin nature of the 2D material makes the finite volume method for numerical calculations infeasible because of the extremely fine meshes required that would lead to long computation times. Instead, the computational model is used to determine the surface temperature rise of the substrate under 0.1 mW laser energy absorption. Then, the temperature difference induced by the interfacial thermal resistance between the 2D material and the substrate is calculated analytically ($\Delta T_{interface} = R''_{tc} q''$) assuming the same heat flux (i.e., absorbed laser energy) from the simulation. Fig. 2a shows how the WSe_2 monolayer temperature rise can then be treated as a sum of the substrate surface temperature and the interfacial temperature difference.

The spatial temperature distribution at both the SiO_2 surface and in the 2D material follow a Gaussian distribution due to the Gaussian nature of the incident laser on the sample. Fig. 2b highlights the higher temperature of the WSe_2 monolayer and smaller temperature of the substrate surface. The laser energy is absorbed and conducted through the 2D material first, causing a temperature rise. Then, as the heat is conducted across the interface and into the substrate, a smaller temperature rise is induced. Note the dissipation of the laser induced temperature rise in the substrate shown as a temperature contour in the cross-plane direction of the substrate. The temperature reaches a maximum at the top surface of the fused silica substrate and gradually cools down further into the material.

The spatial treatment of heat conduction is the same in both CW and ns cases. In the ns case alone, the temperature distribution in the time domain obeys similar behaviour. As shown in Fig. 2c, after multiple ns laser pulses, the gradual heat accumulation reaches a baseline, constant temperature. During a single ns pulse, the temperature profiles of the 2D material and substrate surface follow the same Gaussian relationship due to the Gaussian nature of the laser pulse – again, the WSe_2 layer receiving the absorbed laser energy first and experiencing a higher temperature rise compared to the underlying substrate. Note that the difference between the temperature rise in the 2D material and the substrate – featured in Fig. 2d – is the analytically solved for interfacial temperature difference. As shown in Fig. 2e, this temperature difference also follows a Gaussian distribution.

The formulation of the ET-Raman method uses numerical modelling to evaluate the substrate temperature rise. For ns laser heating case, sufficient laser pulses are simulated to capture the heat accumulation effect. Then, the temperature rise of the supported WSe_2 monolayer is solved for analytically using the solved integral equations from above. To evaluate the Raman intensity weighted average integral, it is necessary to use the basic formula relating the temperature difference across an interface to the local heat flux q'' and interfacial resistanceR''_{tc}: $T_{\mathrm{WSe}_2} - T_{\mathrm{SiO}_2} = R''_{tc} q''$. In this way, the temperature rise of the sample can be shown to be $\overline{T}_{WSe_2,CW} = aR''_{tc} I_0/2 + \overline{T}_{SiO_2,CW}$ where $\overline{T}_{SiO_2,CW}$ is the Raman intensity weighted average temperature rise of the fused silica substrate under CW heating solved for via numerical modelling and a is the laser absorption. Similarly, for the ns case the weighted average can be evaluated as $\overline{T}_{WSe_2,ns} = aR''_{tc} I_0/(2\sqrt{2}) + \overline{T}_{SiO_2,ns}$ where I_0 becomes the ns laser intensity and $\overline{T}_{SiO_2,ns}$ is the average temperature rise of the fused silica under ns heating. Theoretically, the temperature rise of the 2D material can be directly calculated in numerical modelling. However, since the 2D material is extremely thin (~nm), including it directly in the numerical modelling would require extremely fine meshes, making the computation very time consuming.

4. Effect of transient heating pulse width on *G* measurement

As detailed in our earlier work, it is shown that by equating the temperature rise ratio $\overline{T}_{WSe_2,ns}/\overline{T}_{WSe_2,CW}$ with the Raman shift coefficient ratio ψ_{ns}/ψ_{CW} where ψ_{ns} and ψ_{CW} are the laser power differentials from respective laser sources, one can solve for the interfacial thermal conductance G. In the context of this sensitivity study, the value of interest becomes the ratio ψ_{ns}/ψ_{CW} which will be defined as the normalized Raman shift coefficient Θ.

The advantage of this technique is the ability to vary the ns laser pulse features in the simulation, namely the pulse width and repetition rate, and observe the different thermal responses in the 2D material-substrate system. This approach also allows for easy exploration of the resistance R''_{tc} effect on interfacial thermal transport. The other necessary parameters involved in this methodology are the thermophysical and optical material properties used for the 3D numerical modelling of laser-induced heat conduction: Volumetric heat capacities of WSe_2 and glass ($\rho c_p = 1.98 \times 10^6$ and $\rho c_p = 1.65 \times 10^6$ J m^{-3} K^{-1}, respectively); thermal conductivity of glass ($k = 1.4$W m^{-1} K^{-1}); and extinction coefficient of WSe_2 ($k_L = 1.28$) [27–30]. In addition, the CW and ns laser properties used in this modelling are listed here: Both with wavelength $\lambda = 532$ nm; CW laser spots sizes at respective objective lenses of $r_{20\times,CW} = 1.8$, $r_{50\times,CW} = 0.7$, $r_{100\times,CW} = 0.4$ µm; and ns laser spot sizes of $r_{20\times,ns} = 1.0$, $r_{50\times,ns} = 0.4$, $r_{100\times,ns} = 0.25$ μm. These spot

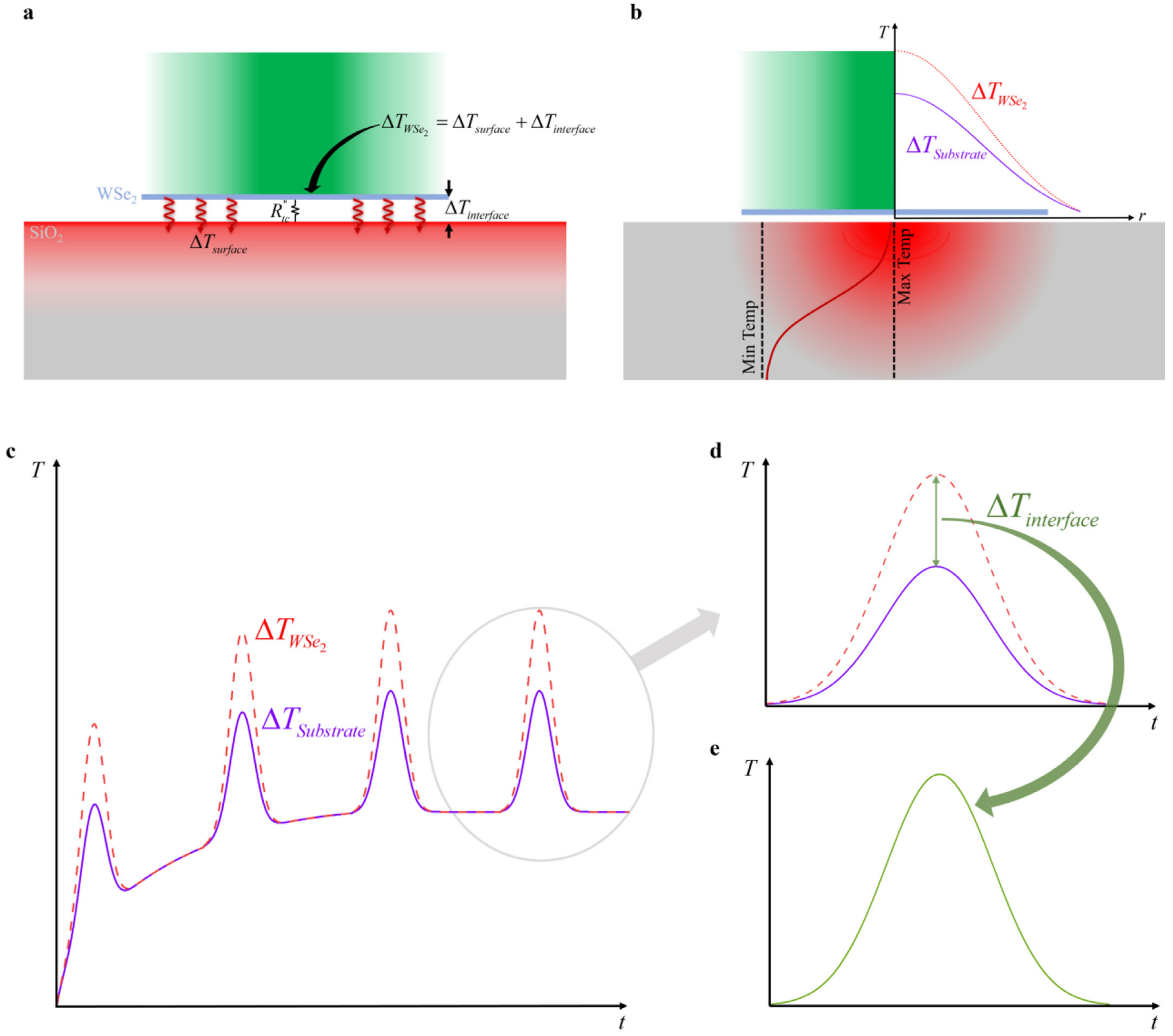

Fig. 2. Spatial and temporal considerations of laser induced heating for the CW and ns cases. (a) The supported 2D material temperature rise is calculated as the sum of the substrate surface temperature (from numerical modelling) and the temperature difference induced by the interfacial thermal resistance (calculated analytically). (b) The WSe$_2$ monolayer experiences a higher temperature rise than the substrate and follows a Gaussian spatial distribution. Additionally, the temperature profile in the cross-plane direction is shown in the substrate. (c) In the ns case, accumulated heating causes the temperature profile to gradually increase until reaching a constant baseline temperature. In the time domain, the laser pulse causes the monolayer to have a larger temperature increase than the underlying substrate. (d) and (e) Show the temporal temperature profile during a single ns pulse where the interfacial temperature difference between the 2D material and the substrate also follows a Gaussian distribution.

sizes reflect the numbers measured in our previous experiments [21].

The final remarks regarding the parameters used for numerical modelling are related to the pulse width t_0 and monolayer thickness z. In our treatment, the pulse width t_0 is defined by the time at which the laser pulse intensity is e^{-1} of its maximum value. The laser spot radius r_0 on the sample surface is defined in the same way using e^{-1} of the maximum value of the laser intensity in the spatial domain. Therefore, the laser intensity distribution for the ns laser in time and space for ns laser heating is fully defined as $I = I_0 \exp(-r^2/r_0^2)\exp(-t^2/t_0^2)\exp(-z/\tau_L)$. As to the sample thickness z, WSe$_2$ monolayers have been measured as 0.7 [31] and 1.1 nm [32]. The ratio analysis involved in the ET-Raman method ensures that the RSC does not depend on sample thickness. For our simulation purposes, a thickness of 0.7 nm is used.

The 2D contour plots shown in Fig. 3a illustrate how the ns laser pulse width t_0 and interfacial thermal conductance G are related to sample temperature rise when pulse repetition rate is set at 300 kHz. A sampling range of pulse widths and conductance values confirms that low conductance and short pulse widths cause the greatest temperature increase in the 2D layer. Furthermore, this same behaviour applies to the normalized Raman shift coefficient Θ (Fig. 3b). Note the accelerating growth in temperature rise and Θ as the pulse width reduces to 20 ns or less. The plotted simulation results assume a 0.1 mW incident laser intensity that is completely absorbed – an arbitrary parameter choice that means the numerical temperature rise and Θ themselves have no inher-

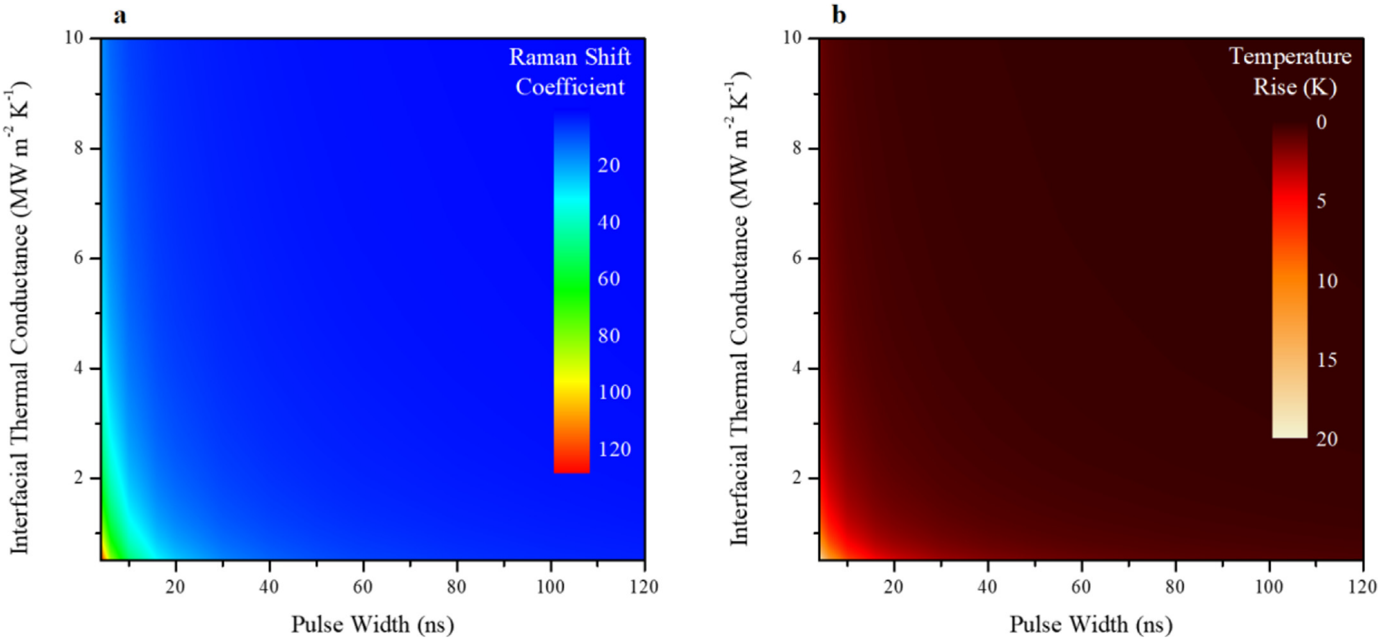

Fig. 3. 2D contours of the (a) temperature rise and (b) Raman shift coefficient when the ns laser pulse width and G are independent variables for numerical modelling and analysis.

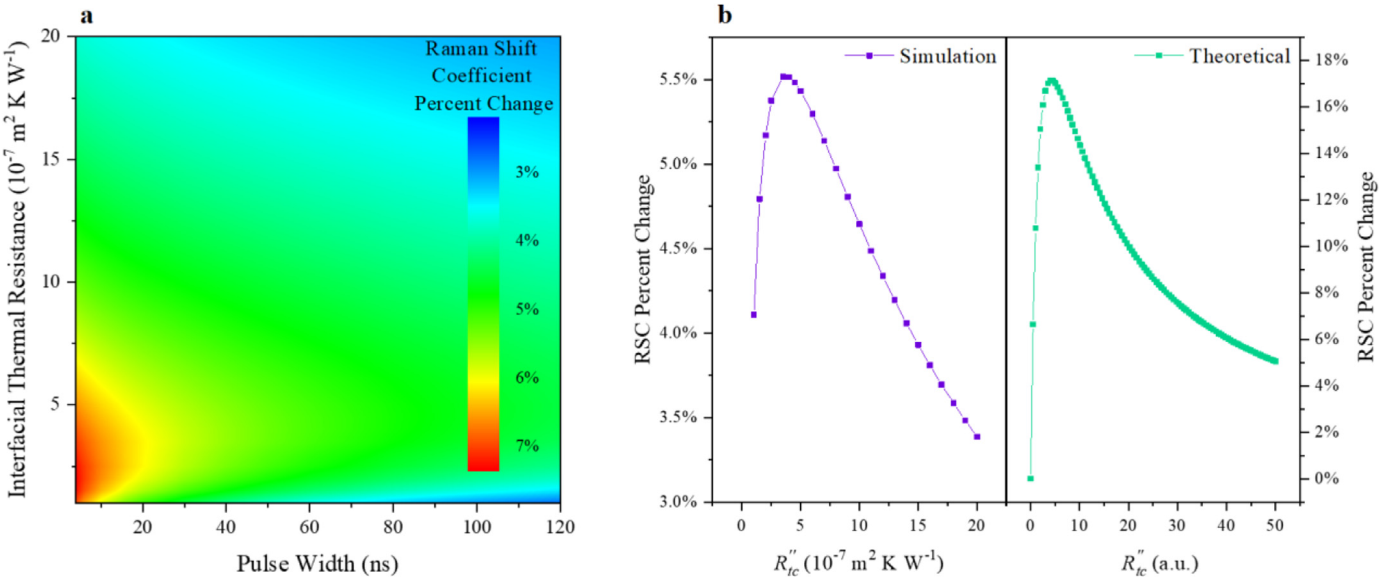

Fig. 4. (a) 2D contours of the sensitivity of the Raman shift coefficient to a 10% change in interfacial thermal resistance. The region of highest sensitivity corresponds to short pulse widths and small resistance values. (b) For a fixed pulse width of 40 ns, the simulation results show a non-monotonic relationship between RSC sensitivity and R''_{tc}. A simplified approach to the modelling analysis corroborates this relationship.

ent value. Their usefulness comes from observing their functional behaviour as other parameters change (i.e. t_0 and R''_{tc}).

In this case, the relevant relationship is between interfacial resistance and the normalized Raman shift coefficient which, as stated previously, can be equated to the ratio of simulated 2D layer temperature rises from ns and CW laser heating: $\Theta = \overline{T}_{WSe_2,ns}/\overline{T}_{WSe_2,CW}$. In particular, it is worth understanding how small changes in R''_{tc} impact the simulated temperature rises and subsequent Θ value. This relationship will inform on how sensitive the experimentally determined Θ is at providing precise measurements of R''_{tc}. To study this relationship, a 2D contour with $t_0$and R''_{tc} as independent variables (Fig. 4a) shows the percent change in Θ after a 10% increase inR''_{tc}. The regions of largest percent change in Θ indicate the most sensitivity to meaningful interfacial thermal resistance measurements. As Fig. 4a details, shorter pulse widths correspond to greater percent changes in Θ, and therefore enhanced potential for precise R''_{tc} measurements. This trend aligns with our earlier hypothesis: A shorter pulse width contributes to a smaller thermal diffusion length and subsequent reduced substrate resistance. As the heat transfer effect from the substrate diminishes, the heat transfer across the interface becomes more detectable by ET-Raman.

The non-monotonic behaviour of the sensitivity evident in the 2D contours in Fig. 4a is an unexpected result deserving of further attention. To confirm and interpret the physics of this trend, we derive a simple physical model for order analysis to track the percent changes in Θ for unit percent change inR''_{tc}. The normalized Raman shift coefficient is written in terms of the laser spot

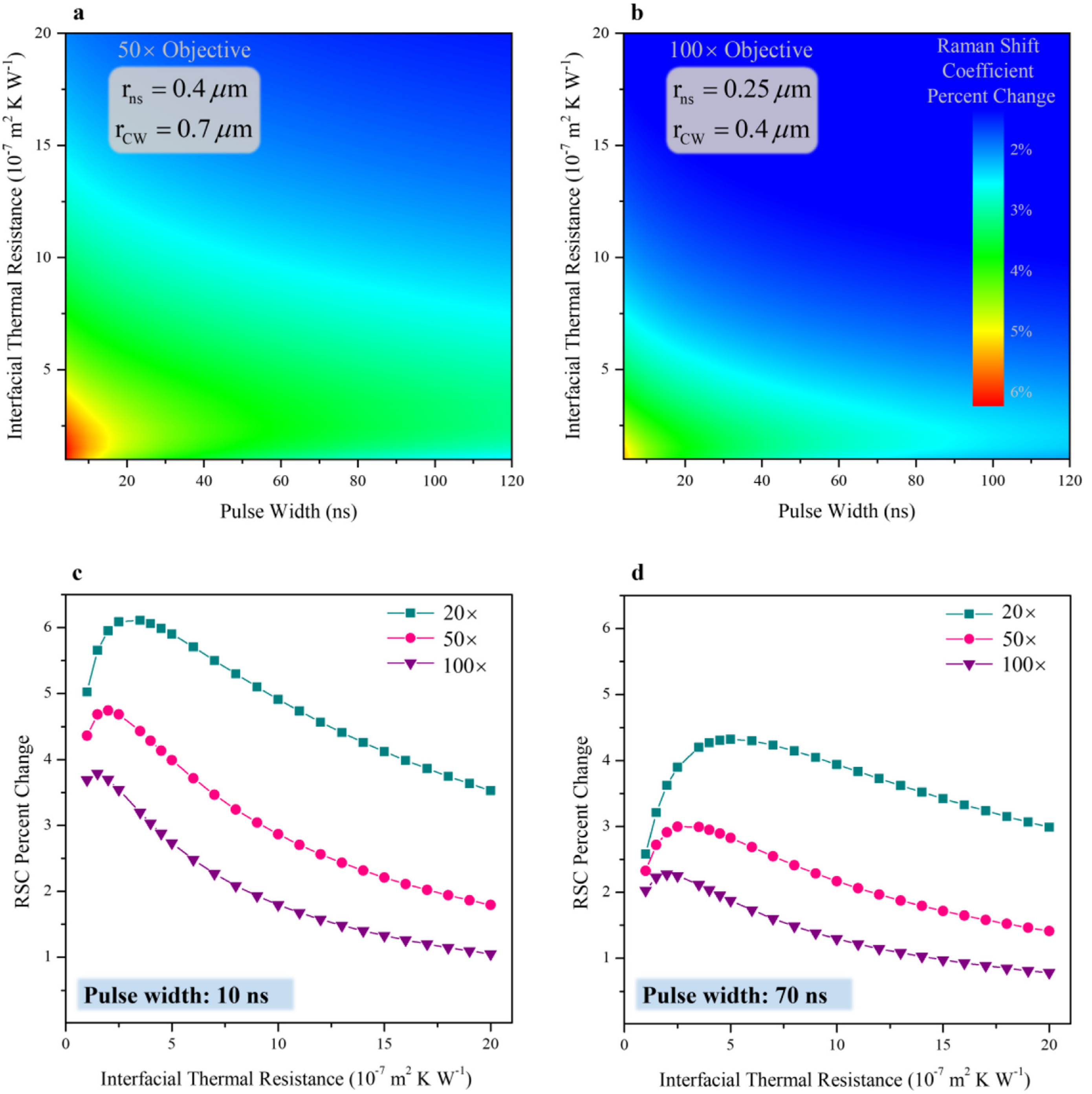

Fig. 5. 2D contours of the RSC sensitivity to 10% changes in R''_{tc} for the (a) 50× and (b) 100× objective lens. As the laser spot becomes smaller, the RSC becomes less sensitive to changes in resistance. Note the colour bar applies to both 50× and 100× contours. (c) and (d) show curves extracted from the 2D sensitivity contours at fixed pulse widths of (c) 10 ns and (d) 70 ns for all three objective lenses. For any given pulse width, the sensitivity of the RSC decreases with increasing R''_{tc}. Note that the RSC percent change increases for small R''_{tc} until reaching a maximum point after which the sensitivity declines. These curves illustrate how the sensitivity dulls as laser pulses broaden and as the objective size increases (i.e. laser spot size reduces).

diameter D, R''_{tc}, and arbitrary constant coefficients associated with heating at the substrate and interface: $\Theta = \frac{aD^{-2}+bR''_{tc}D^{-2}}{fD^{-1}+gR''_{tc}D^{-2}}$. The numerator consists of the ns temperature rises due to the substrate resistance (aD^{-2}) and the interfacial resistance ($bR''_{tc}D^{-2}$). The denominator represents the induced temperature rises at the substrate (fD^{-1}) and interface ($gR''_{tc}D^{-2}$) under CW laser heating. This modelling follows the reasoning delineated earlier in Section 2 of this paper.

The next step in modelling analysis involves writing the percent changes of Θ and R''_{tc} as differentials. These can be approximated as $\frac{\Delta\Theta}{\Theta} = \frac{\partial\Theta}{\Theta}$ and $\frac{\Delta R''_{tc}}{R''_{tc}} = \frac{\partial R''_{tc}}{R''_{tc}}$. Therefore, the percentage change in Θ for a unit percentage change in R''_{tc} can be evaluated as $\frac{\Delta\Theta/\Theta}{\Delta R''_{tc}/R''_{tc}} = \frac{\partial\Theta}{\partial R''_{tc}} \times \frac{R''_{tc}}{\Theta}$. Plotting this function for a range of interfacial resistance values with arbitrarily assigned constants and laser spot diameter demonstrates the same non-monotonic relationship exhibited in the simulation results. Fig. 4b shows

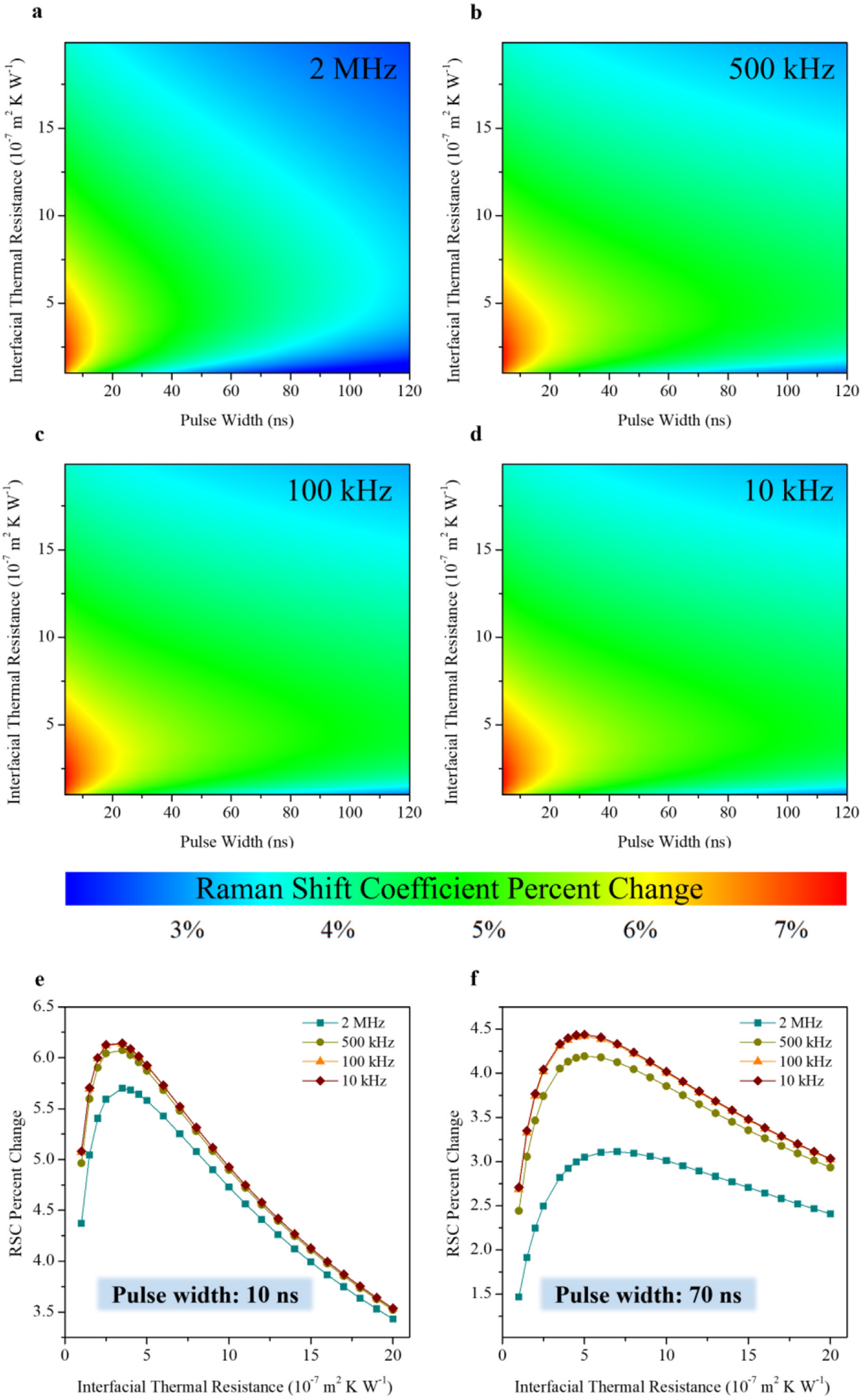

Fig. 6. The 2D sensitivity contours at various ns laser repetition rates showing percentage change in Raman shift coefficient for a 10% change in R''_{tc}. As the pulse frequency decreases from 2 MHz (a) to 10 kHz (d), the range of pulse widths that will detect changes in R''_{tc} with enhanced precision widens. (e) and (f) show extracted curves from the 2D contours at each repetition rate for pulse widths of 10 and 70 ns.

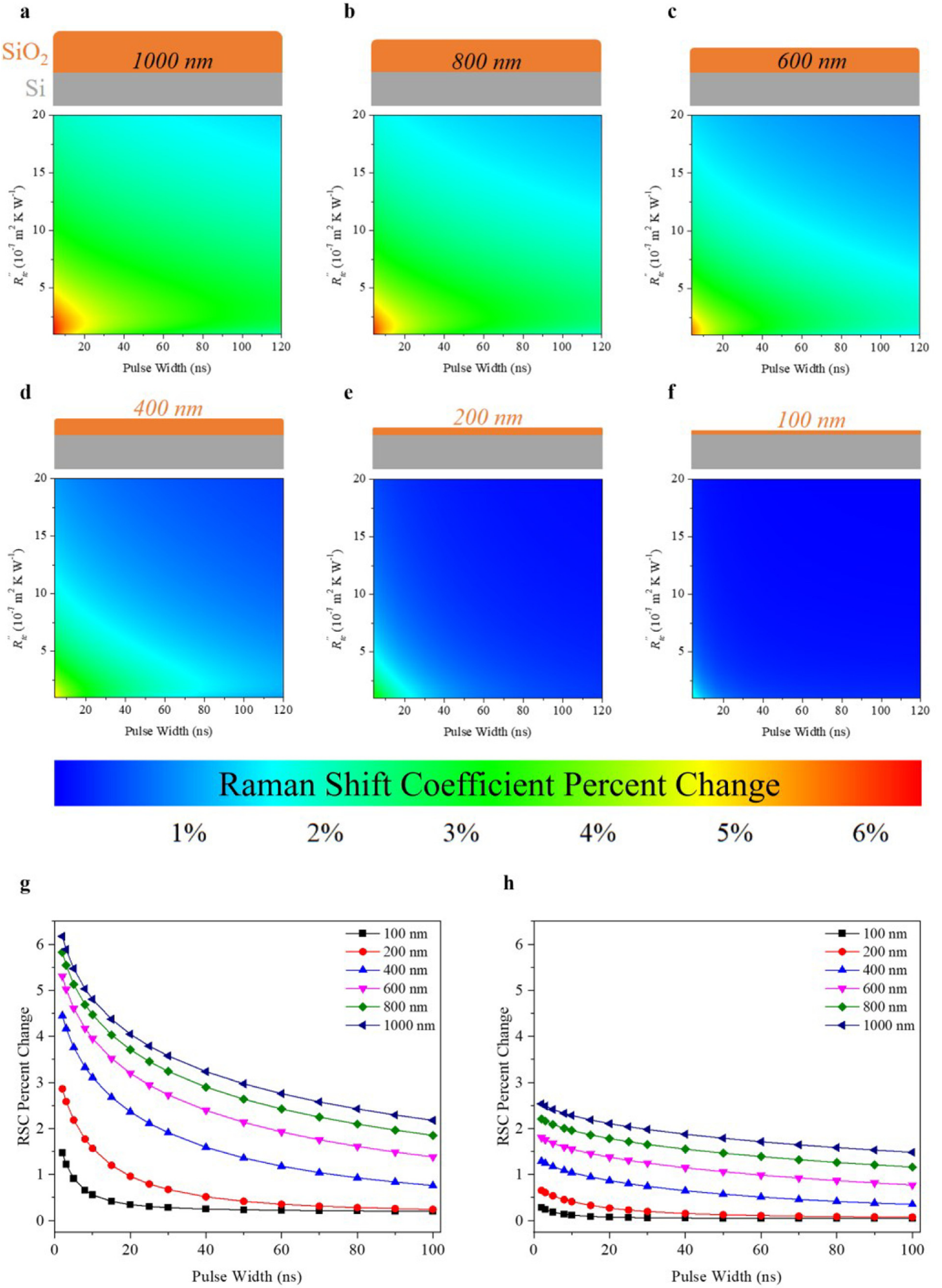

Fig. 7. The 2D sensitivity contours for WSe_2 monolayer samples with SiO_2/Si substrate. (a), (b), and (c) are contours for SiO_2 thicknesses of 1000, 800, and 600 nm, respectively. The Raman shift coefficient registers high levels of sensitivity when the interfacial resistance changes by 10%, with sensitivity improving as the thickness increases. As the oxide thickness decreases to 400 nm (d), 200 nm (e), and 100 nm (f) the Raman shift coefficient fails to detect the 10% changes in R''_{tc} with much precision. (g) and (h) show curves extracted from the 2D contours at different SiO_2 thicknesses for fixed interfacial thermal resistances of 2×10^{-7} m^2 K W^{-1} and 1.5×10^{-6} m^2 K W^{-1}, respectively.

the trend comparison between the derived formula above and the simulation results of an extracted contour curve pulled from Fig. 4a at a pulse width of 40 ns. Conceptually, this trend makes sense considering that an infinitesimally small resistance (essentially zero) at the interface would not be sensitive to any Raman-based measurement approaches. Once a threshold of interfacial resistance is reached, the sensitivity begins to decay as the resistance grows.

The 3D numerical thermal modelling also helps clarify the effect of laser spot size on ET-Raman measurements. Fig. 5 shows two additional sensitivity contour maps for the 50× and 100× objective lens. These lenses shrink the ns laser spot size to 0.4 and 0.25 µm, respectively. Similarly, the CW laser spot size reduces to 0.7 and 0.4 µm. Clearly, the overall sensitivity to detecting changes in interfacial resistance declines with the laser spot size while the general conditions for high sensitivity remain the same – shorter pulse widths and lower resistance values. For example, the maximum RSC percent change to 10% changes in R''_{tc} for all laser spot sizes occurs at the smallest pulse width simulated when $t_0 = 2\,\text{ns}$. Additionally, these maxima correspond to the smallest interfacial resistance values tested: 1.0×10^{-7} m^2 K W^{-1} for the 100× (5.36%), 1.5×10^{-7} m^2 K W^{-1} for the 50× (6.19%), and 2.0×10^{-7} m^2 K W^{-1} for the 20× objective (7.29%). This trend of increasing sensitivity with laser spot size is also true for larger R''_{tc} and wider pulse widths. When $R''_{tc} = 1.5 \times 10^{-6}$ m^2 K W^{-1} and $t_0 = 80$ ns, the RSC percent change is 0.95% for 100×, 1.68% for 50×, and 3.35% for 20×. This result is seemingly counterintuitive given that the interface effect becomes more pronounced as laser spot diameter decreases. It is suspected that the effect of a smaller sampling area in the radial spatial domain offsets the enhanced heat transfer effect at the interface. In other words, a laser spot focused with a 20× objective covers a greater contact area between the 2D layer and substrate making larger diameter laser spots more likely to probe interfacial effects. The physics behind this observation can be further explained here: When the laser spot size D shrinks, the total interface resistance quickly goes up following the order of D^{-2} while the thermal resistance of the substrate goes up following the order of D^{-1} in both CW and ns laser heating cases (when D is very small, the transient heat transfer is rather three-dimensional in ns laser heating and the total resistance of substrate is proportional to D^{-1}). This makes the thermal resistance of the substrate much less important in the CW and ns laser heating conditions. Therefore, the resulting Θ is much less affected by the heat transfer in the substrate. An extreme case would be when D approaches zero, Θ would go to unity, regardless of R''_{tc} value. Any change in R''_{tc} will not change Θ, leading to the lowest sensitivity of measurement.

The effect of the laser pulse width and laser spot size on RSC sensitivity can be further explained by examining extracted curves from the 2D sensitivity contours at fixed pulse widths. As shown in Fig. 5c,d, the same non-monotonic relationship between RSC percent change and R''_{tc} explained earlier in this section is evident when the pulse width is set to 10 ns (c) and 70 ns (d) for all three objective lenses. Note the increasing responsiveness of the RSC to changes in R''_{tc} as laser spot magnification decreases from 100× to 20×. Additionally, these same plots highlight the inverse relationship between RSC sensitivity and pulse width. For the 20× objective case, when $t_0 = 10$ ns the maximum RSC percent is 6.11% which occurs at $R''_{tc} = 3.5 \times 10^{-7}$ m^2 K W^{-1}. At the same value of R''_{tc}, the RSC percent change for the 70 ns pulse width is only 4.20%. This trend of decreasing sensitivity as the laser pulse width increases holds true for all magnifications and is exemplified in more detail for all the lenses in Fig. 5c,d.

5. Effect of cooling time between laser heating pulses on *G* measurement

The repetition rate of the ns pulsed laser also influences the efficacy of experimental ET-Raman measurements of interfacial thermal conductance. To study the effect of pulse repetition frequency, multiple simulations were done at a range of frequencies from 10 kHz to 2 MHz. It was expected that high frequency pulsing would push the induced heating in the sample towards steady state (similar to CW heating) since the cooling time between consecutive pulses would be too short for the sample to return to ambient room temperature conditions. This would undoubtedly dull the capacity for sensitive interfacial resistance measurements since ET-Raman depends on sufficiently differentiated thermal transport processes.

The 2D contours of percent change in Θ for a given percent change in R''_{tc} ultimately confirm this hypothesis. Fig. 6 shows contours for a range of repetition rates. Again, it can be seen that shorter pulse widths guarantee higher levels of sensitivity no matter the repetition rate. Also, the same range of resistance values, from 1×10^{-7} to 7×10^{-7} m^2 K W^{-1}, remain the most predisposed to precise R''_{tc} measurement. The noticeable trend as the repetition rate increases is the shrinking of the high sensitivity region in the 2D contours; this region is pushed towards a domain where only the shortest pulse widths can predict precise interfacial resistance values. The red area in the 2D contours corresponds to at least a 7% change in Θ for a 10% change inR''_{tc}. At a pulse repetition frequency of 2 MHz, the pulse width must be at most 12 ns to achieve this degree of sensitivity in ET-Raman measurements. On the other hand, at a repetition rate that allows sufficient cooling time between consecutive laser pulses, such as 300 kHz, the pulse width can be up to 20 ns for the same level of sensitivity.

Fig. 6e,f illustrate more details on the effect of pulse width and repetition rate. Both plots show extracted curves from the 2D sensitivity contours at fixed pulse widths of 10 ns (e) and 70 ns (f). Clearly, the overall responsiveness of the RSC to 10% changes in R''_{tc} diminishes as the pulse width grows. Comparison of these plots also highlights the lower sensitivity of RSC at higher repetition rates. At an interfacial resistance of 5.0×10^{-7} m^2 K W^{-1}, the percent change of RSC for the 70 ns pulse width case decreases from 4.44 to 3.05% as the repetition rate goes from 10 kHz to 2 MHz. Similarly, though to a lesser degree, the percentage change for the 10 ns case goes from 5.92 to 5.78% at the same R''_{tc} value.

The analysis of the effect of pulse repetition frequency on experimental measurements of interfacial thermal resistance confirms that accumulated heating in the 2D material-substrate system from high frequency pulsed lasers must be considered when choosing an appropriate repetition rate. It is preferable to choose a frequency such that the resulting effect of laser irradiation is indeed transient heat conduction rather than effectively steady state heating. Furthermore, choosing a repetition rate that optimizes RSC responsiveness for a given pulse width must be seriously considered as well.

6. Significantly reduced sensitivity for *G* measurement of 2D materials on Sio$_2$/Si substrate

The final consideration in this study concerns the effect of substrate on sensitivity to precise G measurements. The previous analysis looks at samples with a fixed fused silica thickness. This thickness is large enough that heat conduction at the interface between the 2D material and substrate can be isolated and measured. However, many studies of 2D materials involve thermally grown silicon dioxide on silicon as the substrate. In this context, thickness of the dioxide layer can influence thermal transport more strongly and can severely influence how sensitive ET-Raman measurements are at detecting *G*.

When the dioxide layer is small, after initial laser irradiation, phonons and hot electrons reach the SiO_2/Si interface sooner. Then, the heat dissipates rapidly because of the high conductivity of silicon. This means that if the pulse width of the ns laser is too long and the dioxide layer is sufficiently thin, the desired transient heating effect at the 2D material-substrate interface will effectively be equivalent to steady state heating with a CW laser during the entire length of the pulse. For example, when the thickness of the dioxide layer is only 100 nm, using the thermal diffusion length formula from before, the time it takes for heat to be conducted to the silicon layer is only 11 ns. Thus, a laser with a 200 ns pulse width (such as the one used in our previous experimental work) does not provide the necessary time resolution to extract precise measurements of *G* using ET-Raman.

In our sensitivity analysis, we examined the effect of different thicknesses of thermally grown SiO_2/Si substrates in measuring interfacial thermal resistance. The simulation results align with the physics theory outlined above. Fig. 7 shows 2D contours of the sensitivity of the Raman shift coefficientΘ in distinguishing changes in R''_{tc} for SiO_2/Si substrates with varying thicknesses of dioxide. As can be seen in parts (e)–(f), when the dioxide thickness is 400, 200, or 100 nm, the percentage change in Θ for 10% changes in R''_{tc} is mostly trivial: The more sensitive region only involving the shortest of pulse widths (~10 ns) and highest sensitivity levels only possible at sub-nanosecond pulse widths. As the dioxide thickness increases to 600, 800, and 1000 nm as shown in (a)–(c), the Θ sensitivity exhibits marked improvement. Not until the dioxide layer reaches 1000 nm does the sensitivity reach the same degree as in the simulation results for the fused silica substrate (note that nanoscale devices usually necessitate thermally grown dioxide layers smaller than 1 µm). For dioxide thicknesses below 1000 nm, the pulse width should be pushed below 10 ns or preferably sub-ns to ensure Θ values are sensitive to changes in interfacial thermal resistance. Therefore, the timescale involved for very thin dioxide layers requires the use of picosecond or femtosecond lasers.

Fig. 7g,h expand upon these 2D sensitivity contours by looking at the SiO_2 thickness effect through extracted curves at fixed interfacial thermal resistance values. At a relatively low R''_{tc} ($2.0 \times 10^{-7} m^2\ K\ W^{-1}$), RSC percent changes for a ns laser pulse width of 10 ns show sizeable variation across the different thicknesses simulated: The RSC sensitivity at 100 nm thickness is mostly negligible with a 0.56% change for 10% change in R''_{tc} while the sensitivity reaches up to 4.81% at 1000 nm SiO_2 thickness. These extracted curves show that it is possible to achieve decent measurement resolution of R''_{tc} using ET-Raman for appropriately chosen pulse widths and oxide substrate thicknesses. On the other hand, for larger R''_{tc} values, the RSC sensitivity fails to reach the same level of resolution. As shown in Fig. 7h, for a R''_{tc} of $1.5 \times 10^{-6}\ m^2\ K\ W^{-1}$, the RSC percent change never exceeds 2.54% for any combination of SiO_2 thickness or pulse width.

It should be noted that narrowing the pulse width to subnanosecond lengths will introduce additional factors that complicate the nanoscale heat transfer model used to extract *G*. At this timescale, the electron-hole recombination, radiative recombination efficiency, 2D material bandgap, and hot electron lifetime all play larger roles in thermal transport. The sub-ns exciton lifetimes of TMD monolayer materials make electron-hole recombination particularly more salient when designing a reliable physical model [33]. For example, WSe_2 monolayers at room temperature have exciton recombination lifetimes in the range of 1–4 ns [34,35]. This means mathematical modelling of heat transfer must include electrons as primary energy carriers and contributors to the 2D material temperature rise since rates of electron-hole recombination are comparable to the timescale of the laser pulse width. Also, given the photoluminescence of monolayer TMDs, radiative recombination efficiency adds further complexity to modelling since not all laser absorbed energy is distributed as heat [24]. Thus, building a physical model that accurately reflects the energy transfer processes involved during a sub-ns laser pulse requires additional parameters that complicate and prolong data processing.

7. Conclusion

After detailed investigation of the pulsed laser temporal features, we conclude that careful consideration of repetition rate and pulse width can optimize the sensitivity of ET-Raman and enhance the quality of interfacial thermal conductance measurements. Numerical modelling of steady state and transient heating confirms high frequency pulsing and longer pulse widths are more likely to inhibit the ability of ET-Raman to distinguish the heating effect at the 2D material-substrate interface. Additionally, it is shown that larger laser spot sizes are more likely to probe interfacial effects and lead to effective ET-Raman capable of achieving high precision *G* measurements. In fact, it is shown that too small laser spot sizes lead to Raman shift coefficients with little dependency on interfacial thermal resistance. It is also concluded that oxide thickness in Si/SiO_2 substrates can severely influence the potential for meaningful accounting of heat conduction across the boundary between 2D material and substrate. Commonly used Si/SiO_2 substrates must have a sufficient layer of oxide (~1 µm) before *G* can be properly measured. These results reveal that pulsed laser temporal features, laser spot size, as well as substrate thickness deserve special attention when designing experimental Raman-based methods.

Declaration of Competing Interest

The authors declare that they have no known competing financial interests or personal relationships that could have appeared to influence the work reported in this paper.

CRediT authorship contribution statement

Nicholas Hunter: Formal analysis, Conceptualization, Writing – review & editing. **Hamidreza Zobeiri:** Conceptualization, Writing – original draft. **Tianyu Wang:** Formal analysis, Writing – original draft. **Xinwei Wang:** Formal analysis, Writing – original draft.

Acknowledgment

Partial support of this work by National Science Foundation (CBET1930866 and CMMI2032464) and DOE (DE-EE0009126) is gratefully acknowledged.

Supplementary materials

Supplementary material associated with this article can be found, in the online version, at doi:10.1016/j.ijheatmasstransfer.2021.121644.

References

[1] T. Mueller, F. Xia, P. Avouris, Graphene photodetectors for high-speed optical communications, Nat. Photonics 4 (2010) 297–301, doi:10.1038/nphoton.2010.40.
[2] A. Pospischil, M.M. Furchi, T. Mueller, Solar-energy conversion and light emission in an atomic monolayer p–n diode, Nat. Nanotechnol. 9 (2014) 257–261, doi:10.1038/nnano.2014.14.
[3] B. Liu, L. Chen, G. Liu, A.N. Abbas, M. Fathi, C. Zhou, High-performance chemical sensing using schottky-contacted chemical vapor deposition grown monolayer MoS_2 transistors, ACS Nano 8 (2014) 5304–5314, doi:10.1021/nn5015215.

[4] J.D. Renteria, D.L. Nika, A.A. Balandin, Graphene thermal properties: applications in thermal management and energy storage, Appl. Sci. 4 (2014) 525–547, doi:10.3390/app4040525.

[5] H. Song, J. Liu, B. Liu, J. Wu, H.-M. Cheng, F. Kang, Two-dimensional materials for thermal management applications, Joule 2 (2018) 442–463, doi:10.1016/j.joule.2018.01.006.

[6] P. Hopkins, Thermal transport across solid interfaces with nanoscale imperfections: effects of roughness, disorder, dislocations, and bonding on thermal boundary conductance, ISRN Mech. Eng. 1 (2013) 1.

[7] X. Liu, M.C. Hersam, Interface characterization and control of 2D materials and heterostructures, Adv. Mater. 30 (2018) 1801586, doi:10.1002/adma.201801586.

[8] M.D. Losego, M.E. Grady, N.R. Sottos, D.G. Cahill, P.V. Braun, Effects of chemical bonding on heat transport across interfaces, Nat. Mater. 11 (2012) 502–506, doi:10.1038/nmat3303.

[9] The interface is still the device, Nat. Mater. 11 (2012) 91–91, doi:10.1038/nmat3244.

[10] C.-C. Chen, Z. Li, L. Shi, S.B. Cronin, Thermal interface conductance across a graphene/hexagonal boron nitride heterojunction, Appl. Phys. Lett. 104 (2014) 081908, doi:10.1063/1.4866335.

[11] Y. Liu, Z.-Y. Ong, J. Wu, Y. Zhao, K. Watanabe, T. Taniguchi, D. Chi, G. Zhang, J.T.L. Thong, C.-W. Qiu, K. Hippalgaonkar, Thermal conductance of the 2D MoS_2/*h*-BN and graphene/*h*-BN interfaces, Sci Rep. 7 (2017) 43886, doi:10.1038/srep43886.

[12] Y. Yue, J. Zhang, X. Wang, Micro/nanoscale spatial resolution temperature probing for the interfacial thermal characterization of epitaxial graphene on 4H-SiC, Small 7 (2011) 3324–3333, doi:10.1002/smll.201101598.

[13] E. Yalon, Ö.B. Aslan, K.K.H. Smithe, C.J. McClellan, S.V. Suryavanshi, F. Xiong, A. Sood, C.M. Neumann, X. Xu, K.E. Goodson, T.F. Heinz, E. Pop, Temperature-dependent thermal boundary conductance of monolayer MoS_2 by Raman thermometry, ACS Appl. Mater. Interfaces 9 (49) (2017) 43013–43020.

[14] X. Zhang, D. Sun, Y. Li, G.-H. Lee, X. Cui, D. Chenet, Y. You, T.F. Heinz, J.C. Hone, Measurement of lateral and interfacial thermal conductivity of single- and bilayer MoS_2 and $MoSe_2$ using refined optothermal raman technique, ACS Appl. Mater. Interfaces 7 (2015) 25923–25929.

[15] W. Cai, A.L. Moore, Y. Zhu, X. Li, S. Chen, L. Shi, R.S. Ruoff, Thermal transport in suspended and supported monolayer graphene grown by chemical vapor deposition, Nano Lett. 10 (2010) 1645–1651, doi:10.1021/nl9041966.

[16] Q.-Y. Li, K. Xia, J. Zhang, Y. Zhang, Q. Li, K. Takahashi, X. Zhang, Measurement of specific heat and thermal conductivity of supported and suspended graphene by a comprehensive Raman optothermal method, Nanoscale 9 (2017) 10784–10793, doi:10.1039/C7NR01695F.

[17] A. Fan, Y. Hu, H. Wang, W. Ma, X. Zhang, Dual-wavelength flash Raman mapping method for measuring thermal diffusivity of suspended 2D nanomaterials, Int. J. Heat Mass Transf. 143 (2019) 118460, doi:10.1016/j.ijheatmasstransfer.2019.118460.

[18] Y. Hu, A. Fan, H. Wang, W. Ma, X. Zhang, Dual-wavelength flash Raman mapping method for measuring thermal diffusivity of the suspended nanowire, Sci. China Technol. Sci. 63 (2020) 748–754, doi:10.1007/s11431-019-9558-3.

[19] S. Xu, A. Fan, H. Wang, X. Zhang, X. Wang, Raman-based nanoscale thermal transport characterization: a critical review, Int. J. Heat Mass Transf. 154 (2020) 119751.

[20] H. Zobeiri, N. Hunter, R. Wang, X. Liu, H. Tan, S. Xu, X. Wang, Thermal conductance between water and nm-thick WS_2: extremely localized probing using nanosecond energy transport state-resolved Raman, Nanoscale Adv. 2 (2020) 5821–5832, doi:10.1039/D0NA00844C.

[21] N. Hunter, N. Azam, H. Zobeiri, R. Wang, M. Mahjouri-Samani, X. Wang, Interfacial thermal conductance between monolayer WSe_2 and SiO_2 under consideration of radiative electron–hole recombination, ACS Appl. Mater. Interfaces 12 (2020) 51069–51081, doi:10.1021/acsami.0c14990.

[22] R. Wang, H. Zobeiri, Y. Xie, X. Wang, X. Zhang, Y. Yue, Distinguishing optical and acoustic phonon temperatures and their energy coupling factor under photon excitation in nm 2D materials, Adv. Sci. 7 (2020) 2000097, doi:10.1002/advs.202000097.

[23] R. Wang, T. Wang, H. Zobeiri, P. Yuan, C. Deng, Y. Yue, S. Xu, X. Wang, Measurement of the thermal conductivities of suspended MoS $_2$ and MoSe $_2$ by nanosecond ET-Raman without temperature calibration and laser absorption evaluation, Nanoscale 10 (2018) 23087–23102, doi:10.1039/C8NR05641B.

[24] A. Splendiani, L. Sun, Y. Zhang, T. Li, J. Kim, C.-Y. Chim, G. Galli, F. Wang, Emerging photoluminescence in monolayer MoS_2, Nano Lett. 10 (2010) 1271–1275.

[25] W. Zhao, Z. Ghorannevis, K.K. Amara, J.R. Pang, M. Toh, X. Zhang, C. Kloc, P.H. Tan, G. Eda, Lattice dynamics in mono- and few-layer sheets of WS_2 and WSe_2, Nanoscale 5 (2013) 9677–9683.

[26] N.V. Velson, H. Zobeiri, X. Wang, Rigorous prediction of Raman intensity from multi-layer films, Opt. Express 28 (2020) 35272, doi:10.1364/OE.403705.

[27] F.P. Incropera, D.P. DeWitt, Introduction to Heat Transfer, John Wiley & Sons, New York, 2002.

[28] A. Blinder, A. Bolgar, Z.A. Trofimova, Thermodynamic properties of selenides of transition metals, Powder Metall. Met. Ceram. 32 (1993) 234–239.

[29] H.-L. Liu, C.-C. Shen, S.-H. Su, C.-L. Hsu, M.-Y. Li, L.-J. Li, Optical properties of monolayer transition metal dichalcogenides probed by spectroscopic ellipsometry, Appl. Phys. Lett. 105 (2014) 201905.

[30] G.-H. Jung, S. Yoo, Q.-H. Park, Measuring the optical permittivity of two-dimensional materials without *a priori* knowledge of electronic transitions, Nanophotonics 8 (2019) 263–270.

[31] H. Fang, S. Chuang, T.C. Chang, K. Takei, T. Takahashi, High-performance single layered WSe_2 p-FETs with chemically doped contacts, Nano Lett. 12 (2012) 3788–3792.

[32] A.S. Pawbake, M.S. Pawar, S.R. Jadkar, D.J. Late, Large Area chemical vapor deposition of monolayer transition metal dichalcogenides and their temperature dependent raman spectroscopy studies, Nanoscale 8 (2016) 3008.

[33] G. Moody, J. Schaibley, X. Xu, Exciton dynamics in monolayer transition metal dichalcogenides, J. Opt. Soc. Am. B 33 (2016) C39, doi:10.1364/JOSAB.33.000C39.

[34] X.-X. Zhang, Y. You, S.Y.F. Zhao, T.F. Heinz, Experimental evidence for dark excitons in monolayer WSe_2, Phys. Rev. Lett. 115 (2015) 257403, doi:10.1103/PhysRevLett.115.257403.

[35] S. Mouri, Y. Miyauchi, M. Toh, W. Zhao, G. Eda, K. Matsuda, Nonlinear photoluminescence in atomically thin layered WSe_2 arising from diffusion-assisted Exciton-exciton annihilation, Phys. Rev. B 90 (2014) 155449.